OPEN ACCESS
IOP Publishing
Superconductor Science and Technology
Supercond. Sci. Technol. **33** (2020) 034004 (13pp)
https://doi.org/10.1088/1361-6668/ab627c

Effect of the fabrication route on the phase and volume changes during the reaction heat treatment of Nb_3Sn superconducting wires

C Scheuerlein[1], J Andrieux[2], M Michels[1], F Lackner[1], C Meyer[3], R Chiriac[2], F Toche[2], M Hagner[4] and M Di Michiel[5]

[1] European Organization for Nuclear Research (CERN), CH 1211 Geneva 23, Switzerland
[2] Univ Lyon, Université Claude Bernard Lyon 1, Laboratoire des Multimatériaux et Interfaces, UMR CNRS 5615, F-69622 Villeurbanne, France
[3] Bundesanstalt für Materialforschung und –prüfung (BAM), 12489 Berlin, Germany
[4] University of Konstanz, 78457 Konstanz, Germany
[5] ESRF—The European Synchrotron, 38000 Grenoble, France

E-mail: Christian.Scheuerlein@cern.ch

Received 18 August 2019, revised 3 December 2019
Accepted for publication 16 December 2019
Published 20 January 2020

Abstract

Accelerator magnets that can reach magnetic fields well beyond the Nb-Ti performance limits are presently being built and developed, using Nb_3Sn superconductors. This technology requires reaction heat treatment (RHT) of the magnet coils, during which Nb_3Sn is formed from its ductile precursor materials (a "wind and react" approach). The Nb_3Sn microstructure and microchemistry are strongly influenced by the conductor fabrication route, and by the phase changes during RHT. By combining *in situ* differential scanning calorimetry, high energy synchrotron x-ray diffraction, and micro-tomography experiments, we have acquired a unique data set that describes in great detail the phase and microstructure changes that take place during the processing of restacked rod process (RRP), powder-in-tube (PIT), and internal tin (IT) Nb_3Sn wires. At temperatures below 450 °C the phase evolutions in the three wire types are similar, with respectively solid state interdiffusion of Cu and Sn, Cu_6Sn_5 formation, and Cu_6Sn_5 peritectic transformation. Distinct differences in phase evolutions in the wires are found when temperatures exceed 450 °C. The volume changes of the conductor during RHT are a difficulty in the production of Nb_3Sn accelerator magnets. We compare the wire diameter changes measured *in situ* by dilatometry with the phase and void volume evolution of the three types of Nb_3Sn wire. Unlike the Nb_3Sn wire length changes, the wire diameter evolution is characteristic for each Nb_3Sn wire type. The strongest volume increase, of about 5%, is observed in the RRP wire, where the main diameter increase occurs above 600 °C upon Nb_3Sn formation.

Keywords: Nb_3Sn, microstructure, phase transformations, volume changes, x-ray diffraction, differential scanning calorimetry, synchrotron micro-tomography

(Some figures may appear in colour only in the online journal)

1. Introduction

With the present Large Hadron Collider (LHC) [1] superconducting main magnets, Nb-Ti technology has reached its

performance limits. The next generation of high field accelerator magnets, presently being built for the High Luminosity LHC (HL-LHC) upgrade [2, 3] and developed for the Future Circular Collider (FCC) project [4, 5], relies on Nb_3Sn superconductors.

There are three main processes for the fabrication of multifilament Nb_3Sn wires: the Bronze Route, and the internal tin (IT) and powder-in-tube (PIT) processes [6]. Multifilament wires made by the PIT process and by the restacked rod process (RRP), which is one of several IT processes, can achieve the high critical current densities needed for HL-LHC accelerator magnets.

In these conductors the superconducting Nb_3Sn is formed during reaction heat treatment (RHT) with a peak temperature of typically 650 °C. At the end of the RHT, Nb_3Sn is formed by a solid state diffusion reaction, where Sn diffuses into the Nb filaments, which are embedded in a common Cu matrix. The morphology of the polycrystalline Nb_3Sn and its Sn concentration distribution strongly influence the critical current density. Both the microstructure and the microchemistry of Nb_3Sn depend on the fabrication route and on the phase changes prior to Nb_3Sn formation. A thorough understanding of the thermodynamics and the phase transformations during RHT is therefore important for the development of future Nb_3Sn conductors [7]. The current phase diagrams of the Cu-Nb-Sn system are incomplete [8].

A disadvantage of coil RHT is that it implies coil volume changes that are difficult to predict. Indeed, volume changes of the conductor during RHT are a significant challenge in the production of Nb_3Sn accelerator magnets by the wind and react process. The relative conductor volume changes before and after RHT have been reported for different conductor types, and in particular, the relative diameter changes of unconfined wires are readily available. The length changes of unconfined Nb_3Sn wires [9, 10] and cables [11] during the entire RHT procedure have also been reported. Typically, the length of unconfined multifilament wires is slightly reduced during RHT, and their diameter substantially increased.

However, knowledge of the unconfined wire or cable volume changes during RHT is insufficient for the prediction of volume changes of magnet coils during the same RHT, because in a coil the conductor volume changes are influenced by the thermomechanical properties of the other coil constituents, such as wedges and spacers, and of the reaction mould. As an example, the 11 Tesla dipole [12] coil length increases during RHT, despite the fact that the unconfined 11 Tesla dipole RRP Rutherford cable length decreases by about 0.3% [11], and the unconfined RRP wire length is barely affected by RHT [10, 11]. In contrast, the length of the new LHC inner triplet quadrupole (MQXFB) magnet [13] coils made of Rutherford cable with a similar RRP wire is decreased after RHT.

This illustrates that in order to predict the coil volume changes, a deeper understanding is required of the mechanisms of conductor volume changes, and of the effect of the thermomechanical behavior of the mould and other coil constituents, and of the friction coefficients between the various pairs of materials during RHT. Previously we reported the thermomechanical properties of the 11 Tesla dipole magnet constituent materials [14–17]. This paper addresses the mechanisms that cause the conductor volume changes during RHT.

By combining several state-of-the-art *in situ* techniques such as differential scanning calorimetry (DSC), high-energy synchrotron x-ray diffraction (XRD), XRD computed tomography (XRD-CT) and synchrotron micro tomography (μ-CT), we have acquired a unique data set that describes in great detail the phase and microstructure changes during the RHT of RRP and PIT wires suitable for accelerator magnets. An IT wire with a low Sn content has been added in this study, for comparison. The diameter changes of the three wires were measured *in situ* with a dilatometer, and are discussed based on a comparison with the crystalline and liquid phases and void volume evolutions in the same wires and of extracted filaments.

2. The samples

2.1. Internal tin (IT) wire

The IT wire [18] with a nominal diameter of 0.825 mm has comparatively low Sn and Nb contents (the Cu to Sn concentration ratio is approximately 82 wt% Cu and 18 wt% Sn). The wire consists of 19 diffusion centers, with 198 Nb 7.5wt% Ta filaments with a diameter of about 3.4 μm. The filaments with a spacing of less than 1 μm are placed around each of the 19 main Sn pools, which have an approximate diameter of 40 μm. The wire has a common diffusion barrier made of Nb and Ta. The phase and porosity volume changes during RHT of the IT wire are described in reference [19].

2.2. Restacked rod process (RRP) wire

The RRP wire [20] produced by Oxford Superconducting Technology (now Bruker EAS) has a nominal diameter of 0.80 mm and contains 54 Nb–Ta alloy filament bundles, each surrounded by distributed diffusion barriers. The strand has an effective filament diameter of about 80 μm and can reach very high 12 T, 4.2 K non-Cu critical current density values close to 3 000 A mm^{-2}. The Cu to non-Cu volume ratio is 0.92. The phase and porosity volume changes during RHT of this wire are summarized in references [10] and [21].

2.3. Powder-in-tube (PIT) wire

The PIT wire [22] manufactured by SMI (now Bruker EAS) has a nominal outer diameter of 1.25 mm and contains 288 subelements with an approximate outer diameter of 50 μm, which are filled with a powder containing $NbSn_2$ and Sn particles, with a thin Cu liner at the interface between the Nb–Ta tubes and the powder. With optimised RHT, the wire can reach critical current densities above 2 500 A mm^{-2} at 12 T and 4.2 K. A detailed description of the phase changes during RHT of the PIT wire is given in reference [23].

3. Experimental techniques

3.1. Dilatometry

The temperature-dependent radial wire expansion was measured with an electronic, highly vacuum-tight, horizontal pushrod dilatometer (Netzsch DIL402C) equipped with a silica glass sample holder. The pushrod contact force was 0.25 N. The calibration of the experimental setup and correction of the expansion curves was done by multiple measurements of a high-purity platinum wire with a diameter of 1 mm.

The Nb_3Sn wires were heated in an argon atmosphere with a heating rate of 100 °C h^{-1}. Cooling from the peak temperature to RT was performed at a rate of −350 °C h^{-1}.

Dilation measurements were performed with Nb_3Sn wires about 10 mm in length, with unsealed ends. From the cold drawing processes, the multifilament wires contain internal stresses that are partly released during heat treatment. Since the wire ends were unsealed, the internal wire pressure might differ from that in a long wire in a coil. For these reasons, the *in situ* dilation results are considered as relative measurements, showing the wire diameter evolution during the RHT process.

In order to obtain precise absolute wire diameter results, the wire diameters before and after full RHT were measured with a laser micrometer system.

3.2. High-energy synchrotron x-ray diffraction (XRD) and micro-tomography (μ-CT)

XRD measurements have been performed at the high energy scattering beamline ID15A of the European Synchrotron (ESRF). The high flux of monochromatic high-energy photons that can be provided at ID15A, in combination with a fast read-out area detector, enables non-destructive monitoring of the phase changes during RHT of Nb_3Sn superconductors in transmission geometry [10, 19, 23, 24].

At the ESRF ID15A beamline high-energy synchrotron, XRD and fast μ-CT measurements [25] can be combined. In this way, the phase changes and the formation of porosity in the IT [19] and RRP wires [10] were monitored *in situ* during the same heat treatment. The spatial resolution of the μ-CT experiments is in the order of 1 μm.

In situ heating of the Nb_3Sn wires was performed in an inert gas atmosphere ($He–H_2$ mixture) in a dedicated x-ray transparent furnace. For the temperature measurement, a thermocouple was directly attached to the wire sample, and the estimated uncertainty of the temperature measurement is smaller than 5 °C.

3.3. High-energy synchrotron x-ray diffraction computed tomography (XRD-CT)

Spatially resolved *in situ* studies of phase composition have been performed at the ID15A beamline by XRD-CT [26], using a monochromatic E = 40 keV pencil beam with a focal spot size of ∼1 μm × 1 μm. The diffracted x-rays were recorded on a Pilatus 2 M detector.

In order to obtain a spatial resolution in the order of 1 μm, and at the same time to have reasonably short acquisition times, for the XRD-CT experiment a PIT filament with a diameter of about 50 μm was extracted from a non-reacted PIT wire by chemical etching of the Cu matrix in nitric acid. The extracted filament was inserted in a glass capillary through which inert gas could be purged during the entire heat cycle of the XRD-CT experiment, in order to prevent strong sample oxidation. Heating was realized with a hot air blower.

The capillary with the filament was fixed to a goniometer attached to a rotation stage and translation stage. For each CT slice, diffraction patterns were recorded at 60 translations spaced 1 μm across the filament, each with 50 different angular orientations (covering the range 0–180°), corresponding to a total number of 3 000 diffractograms. Each diffraction pattern was recorded in about 10 ms, so the acquisition time of one CT slice was approximately 30 s. This very fast acquisition, using a newly developed XRD-CT continuous scan data acquisition system, enables XRD-CT experiments during *in situ* HT with ramp rates of up to 100 °C h^{-1}.

3.4. Differential scanning calorimetry (DSC)

For all DSC analyses, a DSC 1 from Mettler-Toledo was used. The DSC experimental procedure was identical for the calibration tests and for the PIT, RRP and IT wire samples. Data acquisition and analysis were performed using STARe SW 15.00 software. Heat treatments were carried out at a heating rate of 5 °C min^{-1}, from 25 °C to 700 °C, under an argon flow of 50 ml min^{-1}. A 30 min isotherm at 25 °C under argon flow was added to the program temperature in order to purge the furnace prior to the experiments. Standards used for the control calibration test were indium and aluminum. The calibration tests showed errors below 0.1% for In and Al melting temperatures, and below 0.3% for melting enthalpy (<0.1% for Al and <0.3% for In). The sample wires were cut into lengths of about 1 mm in order to maximize the contact between the wires and the bottom of the crucible, as the temperature measurements were made by a 2D sensor below the crucible. Sample masses of 54.62 mg, 51.38 mg, and 47.09 mg of cut wire parts, for PIT, RRP and IT respectively, were placed separately inside 30 μl platinum crucibles with pierced lids.

The heat flow during the Nb_3Sn wire RHT results from the convolution of several endothermic and exothermic phenomena related to different chemical reactivity pathways. As a consequence, the heat signal is identified in the temperature by the peak maximum position and not the onset temperature of the peak, unless otherwise stated.

3.5. Focused ion beam (FIB) nano-tomography

The spatial resolution of μ-CT experiments is insufficient to resolve the voids formed during RHT of a PIT wire. Therefore, the void distribution in a PIT sub-element has been visualized by FIB nano-tomography. A Zeiss Neon 40EsB dual beam system consisting of a Ga + ion beam for milling

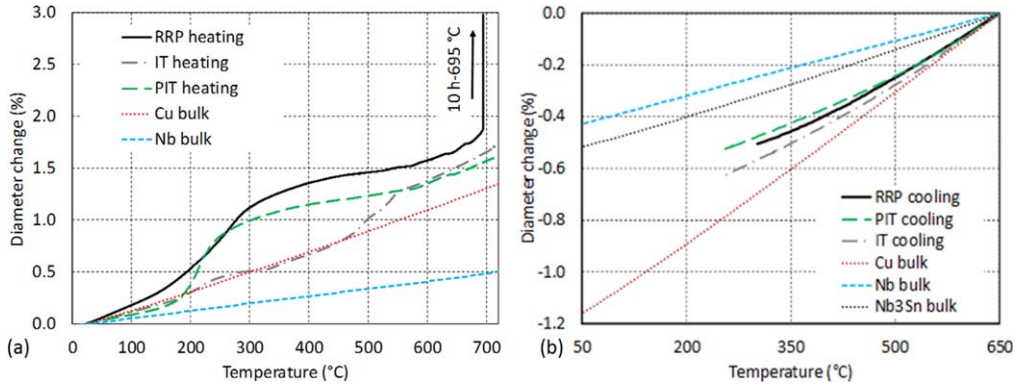

Figure 1. (a) Typical evolution of the RRP, PIT and IT wire diameters as measured by dilation during RHT with a ramp rate of 1.67 °C min^{-1}. (b) Evolution of the reacted RRP, PIT and IT wire diameters during cooling from 650 °C (average of at least two independent measurements). The thermal expansions of Cu, Nb and Nb_3Sn are shown for comparison.

Table 1. Comparison of Nb_3Sn wire diameter and wire and cable length changes before and after RHT. The change to the wire's cross-sectional area was calculated from the diameter change.

	Wire			Cable [11]
	Diameter change (%)	Cross-sectional area change (%)	Length change (%)	Length change (%)
RRP	+2.5	+4.9	−0.07	−0.32
PIT	+1.6	+3.3	−0.15	−0.40
IT	+1.1	+2.3	not measured	not measured

and an electron beam for SEM imaging was used for precise material removal, followed by image acquisition.

Since the field of view is limited, prior to the FIB-SEM experiment a PIT subelement was extracted from the reacted wire by dissolving the Cu stabiliser in nitric acid. Afterwards, the filament was sectioned by the Ga + ion beam. The imaging plane of the SEM is a transverse cross-section of the PIT subelement.

4. Results

4.1. Comparison of Nb_3Sn wire diameter changes during in situ RHT

The diameter, cross-sectional area and length changes of unconstrained Nb_3Sn wires during RHT are compared in table 1 with the length changes of Rutherford cables made of the same Nb_3Sn wire type. The wire volume changes are mainly caused by the increase in the wire's cross-section, which was accompanied by a comparatively small length shrinkage. The wire length change is attributed to relaxation of the unreacted Nb filaments when the Cu matrix is annealed [9, 15, 27]. The length of unconstrained Rutherford cables shrinks by typically 0.3%–0.4% during a standard coil RHT (table 1). The Rutherford cable geometry is described in [11]. The different length changes of Nb_3Sn wire and cable can be partly explained by the untwisting of the Nb filaments in wires [28], which cannot occur in cables.

The diameter evolutions of the IT, RRP and PIT wires during *in situ* RHT with a ramp rate of 1.67 °C min^{-1}, and during cooling with a ramp rate of −5.6 °C min^{-1}, are compared in figures 1(a) and (b), respectively.

During the first heating cycle, the diameter increase deviates from the thermal expansion behavior of the main wire constituents, Nb and Cu. The effect is more pronounced in the RRP wire, and comparatively small in the IT wire (figure 1(a)). In the RRP wire a strong diameter increase occurs during an isothermal 10 h–695 °C plateau, after which Nb_3Sn formation is nearly complete. In the other wire types, Nb_3Sn formation is slower than in the RRP wire, and is not completed.

During cooling, the reacted Nb_3Sn wire diameter thermal shrinkage is between the thermal expansion coefficients of Cu and Nb_3Sn, which are the main constituents of the reacted wires (figure 1(b)).

4.2. Phase changes during RHT as observed by DSC, high-energy synchrotron XRD and XRD-CT

In order to relate heat exchange to chemical reaction, a comparison between DSC and high-energy synchrotron XRD results showing the phase evolution is presented below, for the three Nb_3Sn wire types examined. Complementary metallographic cross-sections obtained by optical microscopy are added, in order to show the radial distribution of the different phases in the wire subelements. For the grinding and polishing of metallographic cross-sections, the wire samples were rapidly cooled from the peak temperature and mounted in a resin for grinding (using silicon carbide papers of 360 grit, 600 grit and 1 000 grit) and polishing (using 9 μm and 3 μm diamond particle suspensions).

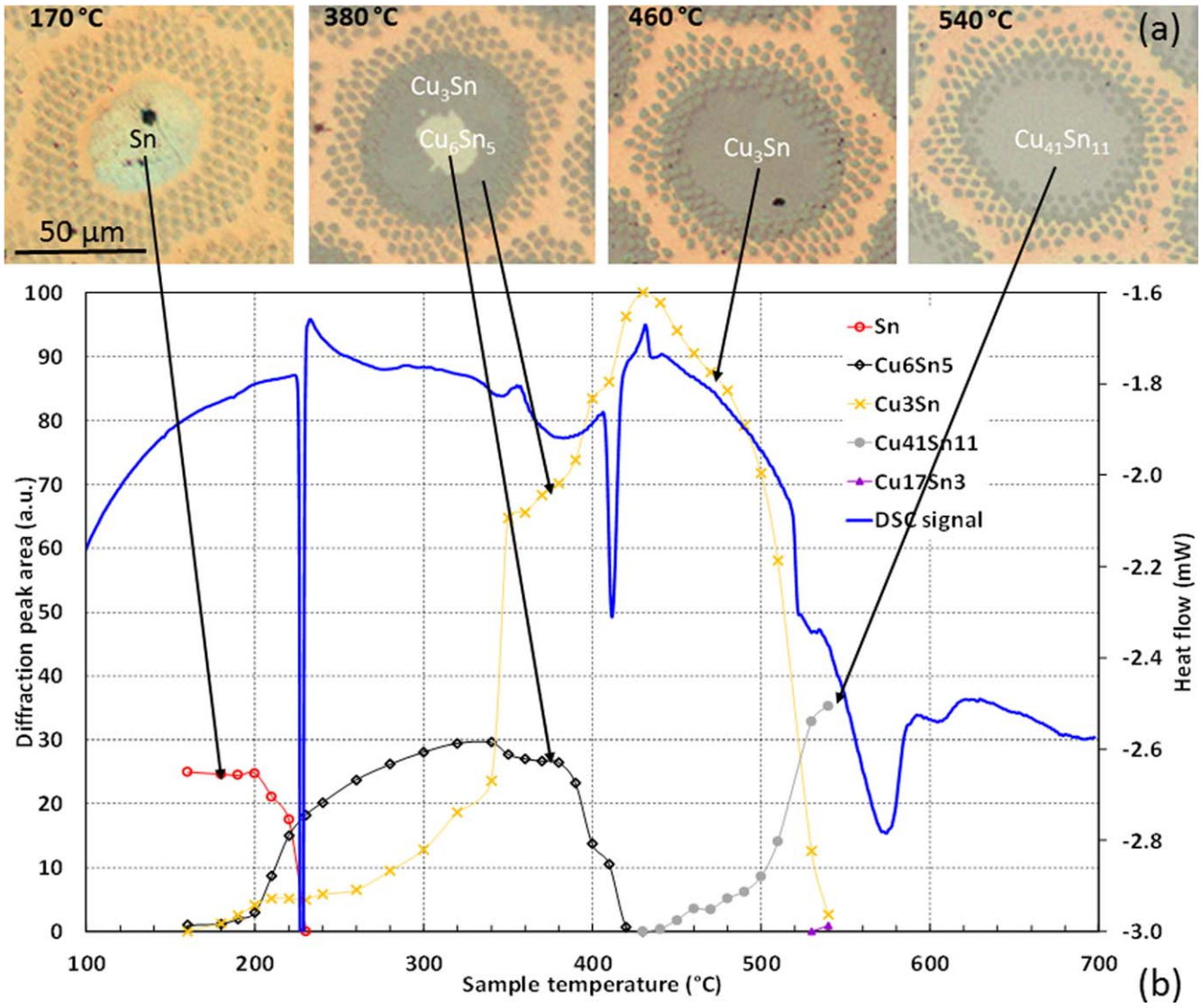

Figure 2. IT wire (a) metallographic subelement cross-sections after 24 h *ex situ* HT to peak temperatures of 170 °C, 380 °C, 460 °C and 540 °C, and (b) comparison of phase evolution (ramp rate 1 °C min^{-1}) and heat flow (ramp rate 5 °C min^{-1}) measured *in situ* by XRD and DSC, respectively.

4.2.1. IT wire. The radial distribution of the different phases retained after cooling from 24 h heat treatment at selected temperatures can be seen in the metallographic cross-sections of an IT wire subelement shown in figure 2(a). The phases Sn, Cu, α-bronze, Cu_6Sn_5, Cu_3Sn, and $Cu_{41}Sn_{11}$ have been identified by energy dispersive x-ray spectroscopy (EDS). The comparison of DSC heat flow and XRD diffraction peak area evolutions for the same wire is presented in figure 2(b).

Solid state interdiffusion of Sn and Cu starts at around 200 °C, as evidenced by the decrease of Sn content and the formation of Cu_6Sn_5 and Cu_3Sn phases, as detected by *in situ* XRD. A first intense and narrow endothermic peak in the DSC signal occurs at 227 °C, which is significantly lower than the pure Sn melting temperature of 231.968 °C [29]. The endothermic peak at 227 °C might correspond to eutectic transformation (Cu_6Sn_5 + (Sn) <-> Liq) [29]. Once the Sn-rich liquid phase is formed, reactivity with Cu might also lead to the formation of Cu_6Sn_5, which, among all the Cu-Sn solid phases, presents the higher driving force of nucleation [30]. Its formation is probably associated with a convoluted exothermic DSC signal at around 231 °C.

With an increasing temperature, the liquid phase Cu composition increases according to the Cu-Sn binary phase diagram [29]. The content of this phase might also decrease in the 250–400 °C temperature range. Indeed, the pure copper constituent is in excess in the wire, leading to a local "out of equilibrium" condition. This drives the global composition to evolve to a higher copper content. As for the Cu-Sn binary phase diagram [29], as the global composition increases in copper, the Liq phase content decreases together with an increase of Cu_6Sn_5 phase content until the limit is reached of the binary Cu_6Sn_5 + Liq phase domain. In other words, the transient liquid phase disappears in the wire at a temperature below 400 °C, as confirmed by the microstructure of the 380 °C metallographic cross-section, and might explain the increase of Cu_6Sn_5 content as measured by *in situ* XRD

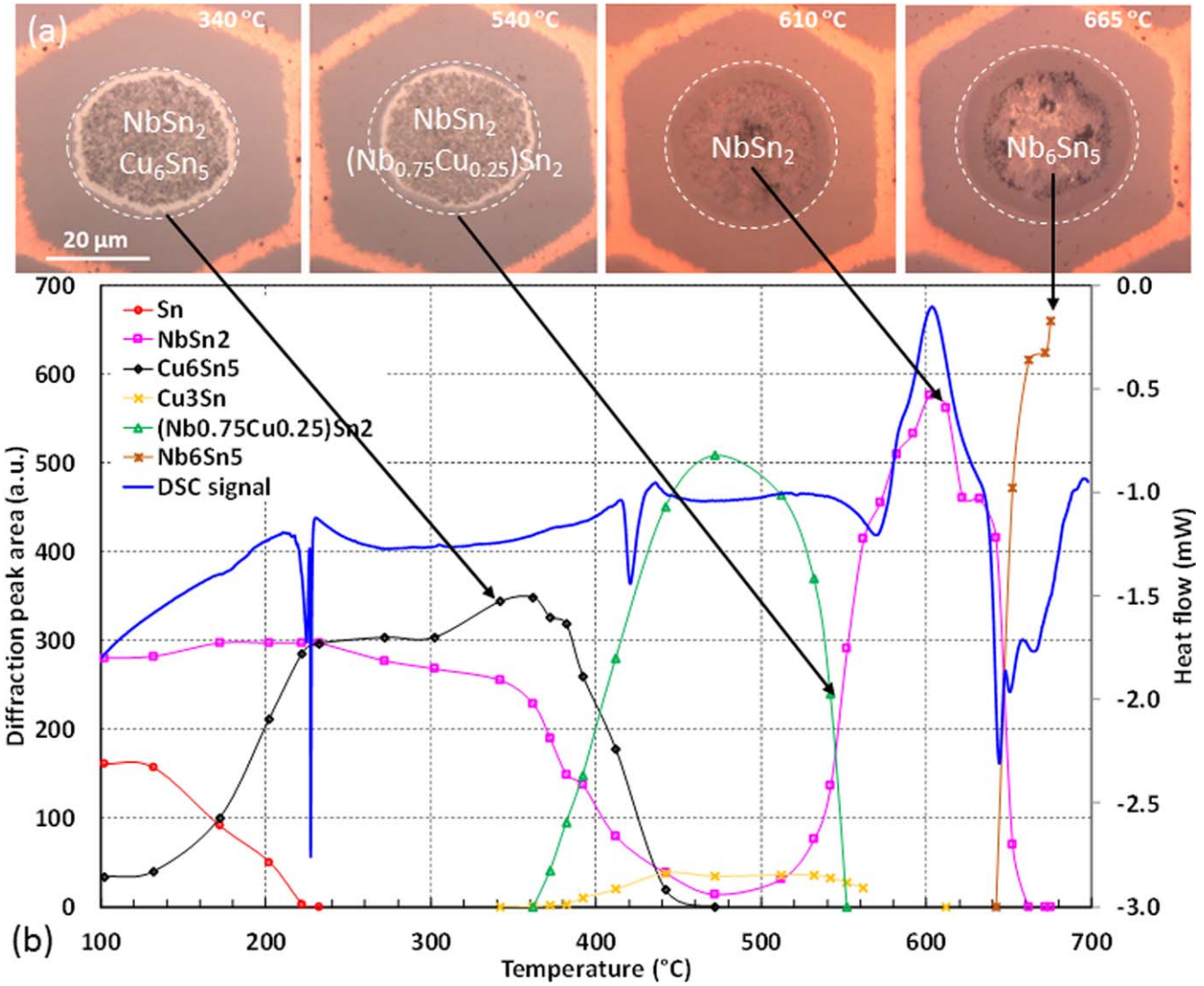

Figure 3. PIT wire (a) metallographic subelement cross-sections after 10 h *ex situ* HT to peak temperatures of 340 °C, 540 °C, 610 °C and 665 °C, and (b) comparison of phase evolution (ramp rate 1 °C min^{-1}) and heat flow (ramp rate 5 °C min^{-1}) measured *in situ* by XRD and DSC, respectively.

(figure 2(b)). The Cu_3Sn content increase observed by *in situ* XRD at around 350 °C might also be explained by the global copper composition evolution by solid state diffusion across the binary $Cu_3Sn + Cu_6Sn_5$ phase domain, given the higher driving force of nucleation of Cu_3Sn at the Cu/Cu_6Sn_5 interface [30].

The endothermic peak at 412 °C ($T_{onset} = 409$ °C) is attributed to Cu_6Sn_5 peritectic transformation according to reaction (1), which is in very good agreement with the transformation temperature of 408 °C reported in [29].

$$Cu_6Sn_5 - > Liq + Cu_3Sn \qquad (R1)$$

The Cu_6Sn_5 peritectic transformation is also evidenced by the *in situ* XRD results, which show a vanishing of the Cu_6Sn_5 phase together with the increase of Cu_3Sn. In the metallographic cross-section of the wire heated to 460 °C it can be seen that Cu_3Sn is the main phase in the subelement (figure 2(a)).

Following reaction (1), a liquid phase is formed at 408 °C. The reactivity of the Liq phase with Cu might also lead to the formation of Cu_3Sn [30] and is probably associated with a convoluted exothermic DSC signal at around 432 °C. This could explain the absence of a Liq phase in the metallographic cross-section at 460 °C. Again, only a global copper composition evolution could explain the change that occurs by solid state diffusion at higher temperature (as detected by DSC and XRD, where the Cu_3Sn content decreases, aiding the $Cu_{41}Sn_{11}$ increase (figure 2(b)). Interestingly, phase transformations and reactivity in the IT wire are mainly driven by Cu and Sn interdiffusion and rely on Cu-Sn binary phase diagram equilibria, at least up to 540 °C, which was the maximum temperature reached during the *in situ* XRD experiment [19].

4.2.2. PIT wire. In figure 3 the evolution of the relative amounts of Sn, $NbSn_2$, Cu_6Sn_5, Cu_3Sn, $(Nb_{0.75}Cu_{0.25})Sn_2$, and Nb_6Sn_5 deduced from the *in situ* XRD results are

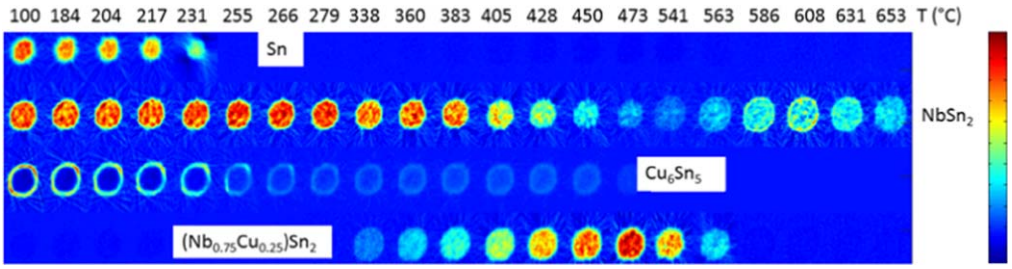

Figure 4. PIT wire radial phase distribution in filament at selected temperatures up to 653 °C, as monitored by XRD-CT during *in situ* RHT. Each column shows the distribution of the phases that could be detected at a certain temperature (pure Sn, $NbSn_2$, Cu_6Sn_5, and $(Nb_{0.75}Cu_{0.25})Sn_2$). The temperatures at which the tomograms were acquired are indicated above each column.

compared with heat flow as a function of the PIT wire temperature.

The solid state interdiffusion of Sn and Cu and the early formation of Cu_6Sn_5 are detected by *in situ* XRD when the temperature exceeds 130 °C. An intense endothermic peak is detected at around 220 °C. In detail, this peak can be decomposed in a first peak at around 224 °C (T_{onset} = 219 °C) followed by a very narrow peak at 227 °C. The latter is attributed to the binary Cu-Sn eutectic transformation [29], whereas the former might be related to ternary Cu-Nb-Sn eutectic transformation: $Cu_6Sn_5 + NbSn_2 + (Sn) <-> Liq$ [31]. The formation of Cu_6Sn_5 by Liq-Solid reactivity between the Sn-rich Liq phase and Cu [30] is probably associated with a convoluted exothermic DSC signal at around 230 °C. At 420 °C (T_{onset} = 415 °C) the observed endothermic peak is attributed to Cu_6Sn_5 peritectic transformation according to reaction (1), as seen by the decrease of Cu_6Sn_5 content together with the formation of Cu_3Sn.

In contrast to the IT wire (figure 2(b)), the simultaneous formation of $(Nb_{0.75}Cu_{0.25})Sn_2$ is evidenced by *in situ* XRD. It is not clear if this formation comes from Cu_6Sn_5 transformation in the presence of Nb or from reactivity between Liq and $NbSn_2$. From a comparison of the work of Li *et al* [32] and Martin *et al* [8], one can expect a $Liq + (Nb_{0.75}Cu_{0.25})Sn_2$ equilibrium at around 430 °C; that is, a stronger argument for $Liq + NbSn_2$ reactivity to form the ternary compound. The formation of $(Nb_{0.75}Cu_{0.25})Sn_2$ does not lead to a clear peak in the DSC signal.

A broad and very intense exothermic peak then occurs at 604 °C and is clearly associated with the formation of $NbSn_2$. This phase might then be transformed in $Liq + Nb_6Sn_5$ from 644 °C and might occur in different steps, as indicated by the three successive detected endothermic peaks. The sequence of formation of phases with increasing temperature (Cu_6Sn_5, Cu_3Sn, $(Nb_{0.75}Cu_{0.25})Sn_2$, $NbSn_2$, and then Nb_6Sn_5) is in very good agreement with equilibria of different phases involving a liquid phase according to the Cu-Nb-Sn ternary system [32]. Moreover, this shows that the composition of the liquid phase evolves in temperature with an increase of the Cu content. Nb_3Sn formation was not detected in the PIT wire, because during the DSC experiment with a ramp rate of 5 °C min^{-1} to 700 °C only a very small amount of Nb_3Sn phase is formed.

The evolution of the radial phase distribution in a Nb_3Sn PIT filament is shown in figure 4. The images have been reconstructed from diffractograms acquired by XRD-CT during *in situ* RHT. As seen in figure 4, the Sn precursor in the PIT filament is no longer detected at temperatures above 231 °C, in agreement with the formation of Cu_6Sn_5 by Liq-Solid reactivity between Liq and Cu [30].

The $NbSn_2$ precursor in the filament core vanishes at about 500 °C. Cu_6Sn_5 is mainly present as a shell at the interface between the Nb tube and its core, or more precisely at the interface between the Cu liner and the $NbSn_2$–Sn powder mixture. In the approximate temperature range of 340 °C to 560 °C, $(Nb_{0.75}Cu_{0.25})Sn_2$ is present across the entire filament core. With increasing temperature, all Sn in the filament is re-transformed into $NbSn_2$, which involves the reaction of part of the inside of the Nb precursor tube. The maximum sample temperature of 653 °C reached during the *in situ* XRD-CT experiment was not sufficient to form Nb_6Sn_5 and Nb_3Sn.

4.2.3. RRP wire. The radial distribution of the different phases retained in the RRP wire after cooling from 10 h heat treatments at selected temperatures is shown in the metallographic cross-sections of figure 5(a), and a comparison of phase evolution deduced from XRD measurements and DSC heat flow is presented in figure 5(b).

Below 500 °C, the phase and heat flow evolution in the RRP wire during thermal treatment (figure 5) is similar to that observed in the IT wire (figure 2(b)). The endothermic peak attributed to the eutectic transformation in the Cu–Sn binary phase diagram [29] is detected at 226 °C. At higher temperatures the Cu_6Sn_5 content increases (as evidenced by XRD and the 340 °C metallographic cross-section) up to 400 °C, due to both Liq + Cu reactivity [30] and global copper composition evolution, as already discussed. The endothermic peak detected at 412 °C (T_{onset} = 408 °C) corresponds to the peritectic transformation of Cu_6Sn_5 to form Cu_3Sn and Liq (reaction (1)), as detected by *in situ* XRD. Some Cu_3Sn is also retained after cooling from 410 °C, as can be seen in the 410 °C metallographic cross-section, which also contains Cu_6Sn_5 reformed during cooling. The formation of the ternary compound and the Nb_2Sn phases are difficult to detect by DSC, due to the relatively low amount of these phases.

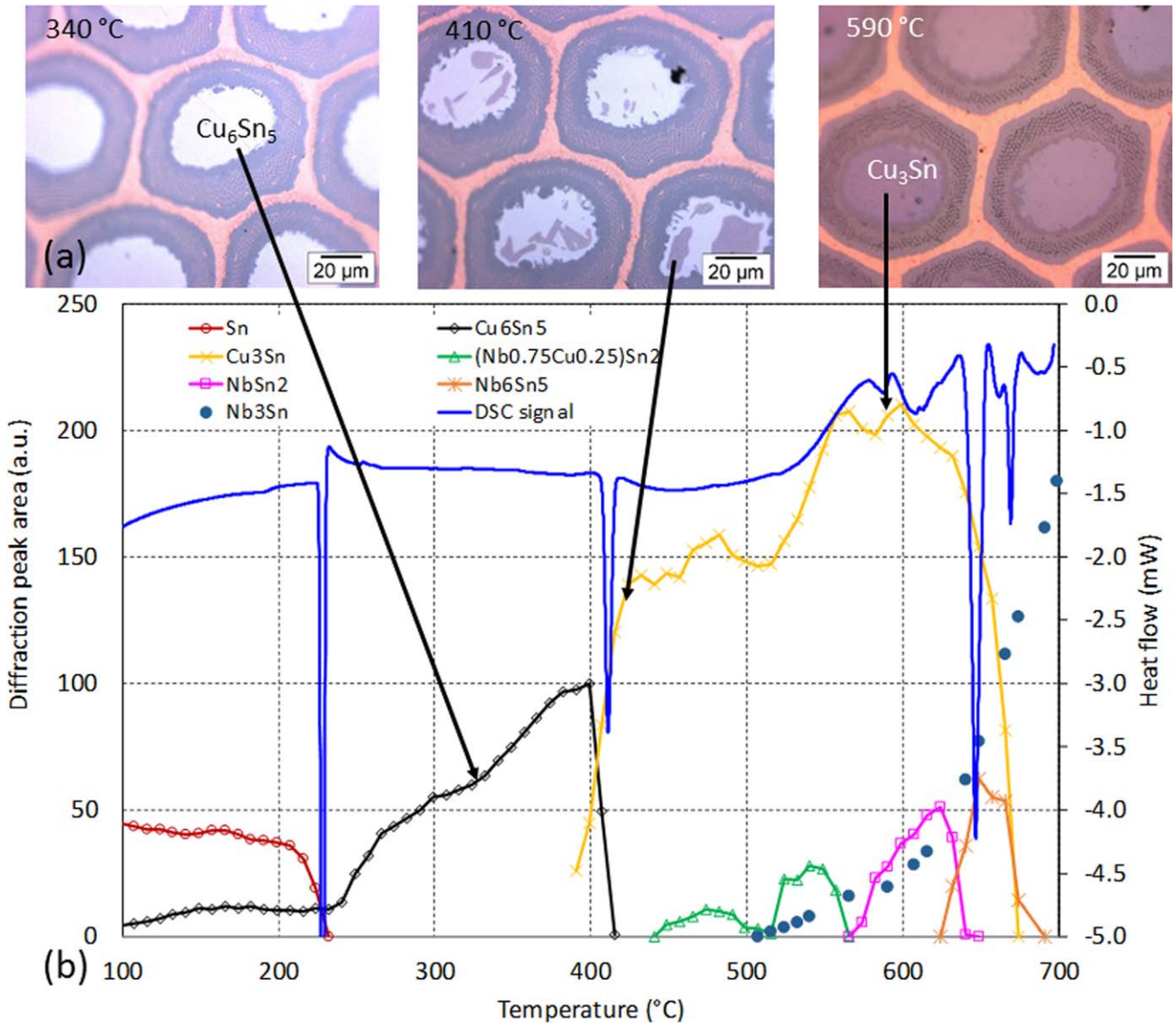

Figure 5. RRP wire (a) metallographic subelement cross-sections after 10 h *ex situ* HT to peak temperatures of 340 °C, 410 °C and 590 °C, and (b) comparison of phase evolution (ramp rate 1 °C min^{-1}) and heat flow (ramp rate 5 °C min^{-1}) measured *in situ* by XRD and DSC, respectively.

Above 500 °C the RRP wire phase changes are similar to those observed in the PIT wire (figure 3). An intense endothermic peak is detected at 647 °C, associated with Nb_6Sn_5 formation. The same phenomenon occurs at 644 °C for the PIT wire. In the RRP wire the onset of Nb_3Sn phase formation is detected at a comparatively low temperature of 500 °C. A strong increase in Nb_3Sn content is detected by *in situ* XRD at around 650 °C, and seems to be correlated to Cu_3Sn and Nb_6Sn_5 decompositions which are related to an endothermic peak at 669 °C (figure 5), also detected for the PIT wire at 665 °C (figure 4).

4.3. Comparison of wire diameter, void volume and phase changes

Below, the porosity volumes and diameter evolutions of the RRP and IT wires during RHT are compared. In these wires the porosity volume could be measured by μ-CT during *in situ* RHT [10, 19]. The voids in the PIT wire are so small that they cannot be resolved by μ-CT experiments. Therefore, FIB nano-CT was applied to visualize the porosity in the fully processed wire.

4.3.1. RRP wire. In figure 6(b) the RRP wire diameter and length evolution during *in situ* RHT are compared with the porosity and Nb_3Sn volume evolution, which were monitored simultaneously by high-energy synchrotron μ-CT and XRD, respectively [10]. Figure 6(a) shows the corresponding 3D reconstructed μ-CT images of the porosity in the RRP wire. In order to expose the porosity inside the wire, all strand materials (liquid and solid) have been transparently depicted.

A first strong void volume increase is observed when the RRP wire temperature exceeds about 220 °C, coinciding with the eutectic transformation (Cu_6Sn_5 + (Sn) <-> Liq), as

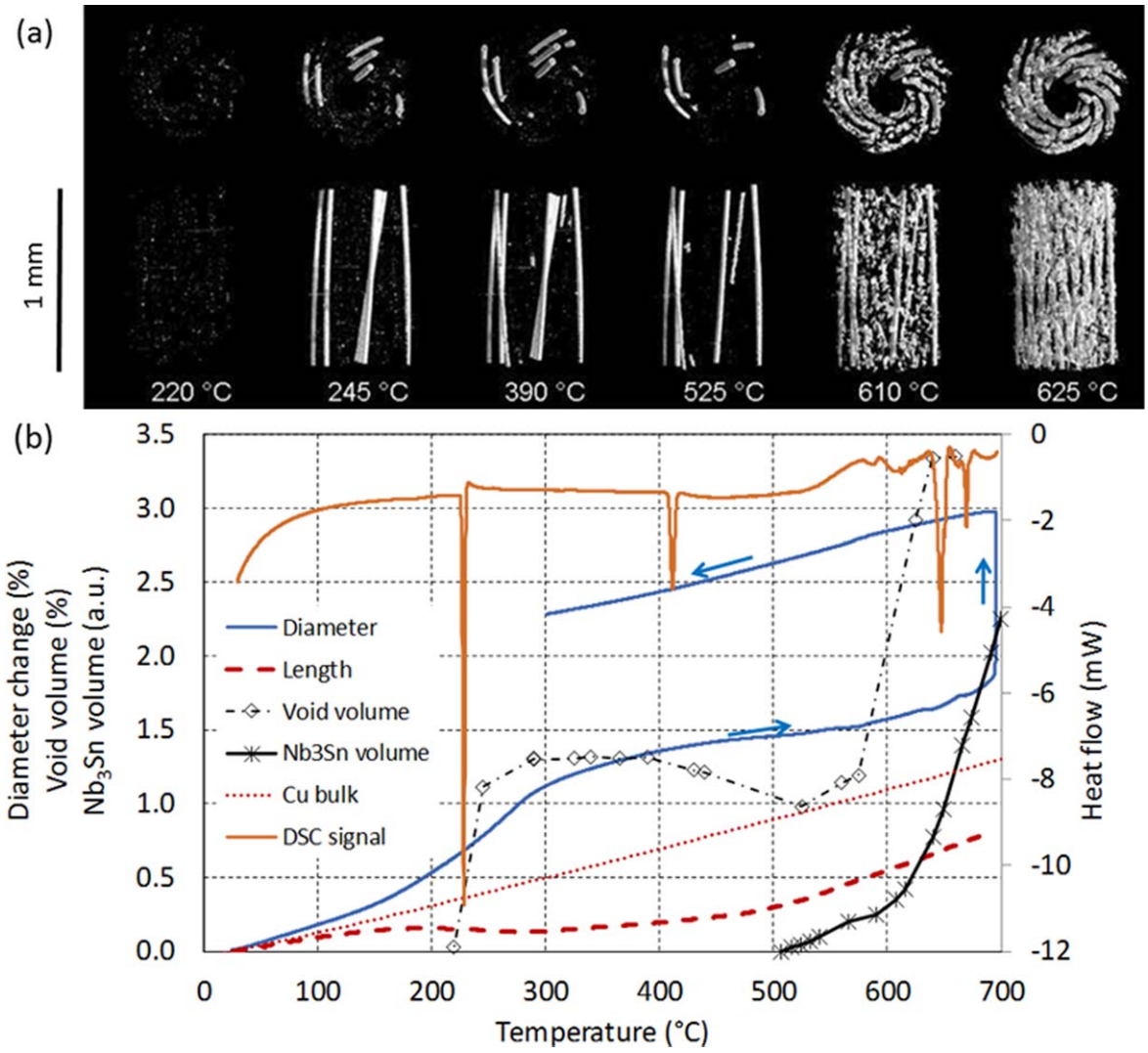

Figure 6. (a) 3D view of the pores in the RRP wire recorded by μ-CT during *in situ* RHT (the strand materials have been transparently depicted). © IEEE. Reprinted, with permission, from [10]. (b) Comparison of the RRP wire diameter and length, pore, and Nb_3Sn volume changes during *in situ* RHT with a ramp rate of 1.67 °C min^{-1} and DSC signal measured during heating at 5 °C min^{-1}. The Cu thermal expansion is shown for comparison.

manifested by the XRD and DSC signals. The peritectic transformation of Cu_6Sn_5 to Cu_3Sn + Liquid (endothermic peak at about 410 °C) strongly affects neither the void volume nor the wire diameter evolution.

Cu is the wire constituent with the highest thermal expansion coefficient. Thus, a wire diameter increase during RHT exceeding the Cu thermal expansion indicates a permanent wire diameter increase. The initial slight diameter increase can be attributed to the simultaneous wire length reduction that is caused by the relaxation of the Nb filaments.

The strongest RRP wire diameter increase occurs above 650 °C, in the temperature range where the XRD results show the disappearance of the high-density Cu_3Sn phase and the formation of Nb_3Sn. The dilation measurements indicate that during a 10 h–695 °C plateau the wire diameter increases by more than 1%.

4.3.2. IT wire. The diameter and void volume evolution in the IT wire are compared in figure 7(b). The corresponding void distribution in the IT wire at selected temperatures is shown in the 3D reconstructed μ-CT images of the pores in figure 7(a). The void volume evolution in the temperature region of 300 °C to 550 °C is caused by the formation of Cu_3Sn, which has a comparatively higher density than its Cu and Sn precursors in the stoichiometric quantities [19]. The strong void volume increase above 300 °C does not cause a diameter increase. Above 550 °C another type of porosity is formed, which is too small to be quantified by the μ-CT experiment [19]. The diameter increase in the temperature interval 450–550 °C is presumably caused by the transformation of Cu_3Sn in the lower density phase $Cu_{41}Sn_{11}$.

4.3.3. Porosity in the reacted PIT wire. The porosity inside the reacted PIT wire is so slight that it cannot be resolved by non-destructive μ-CT experiments. Conventional metallographic preparation usually modifies the fine microstructure of the core, so that the porosity in the

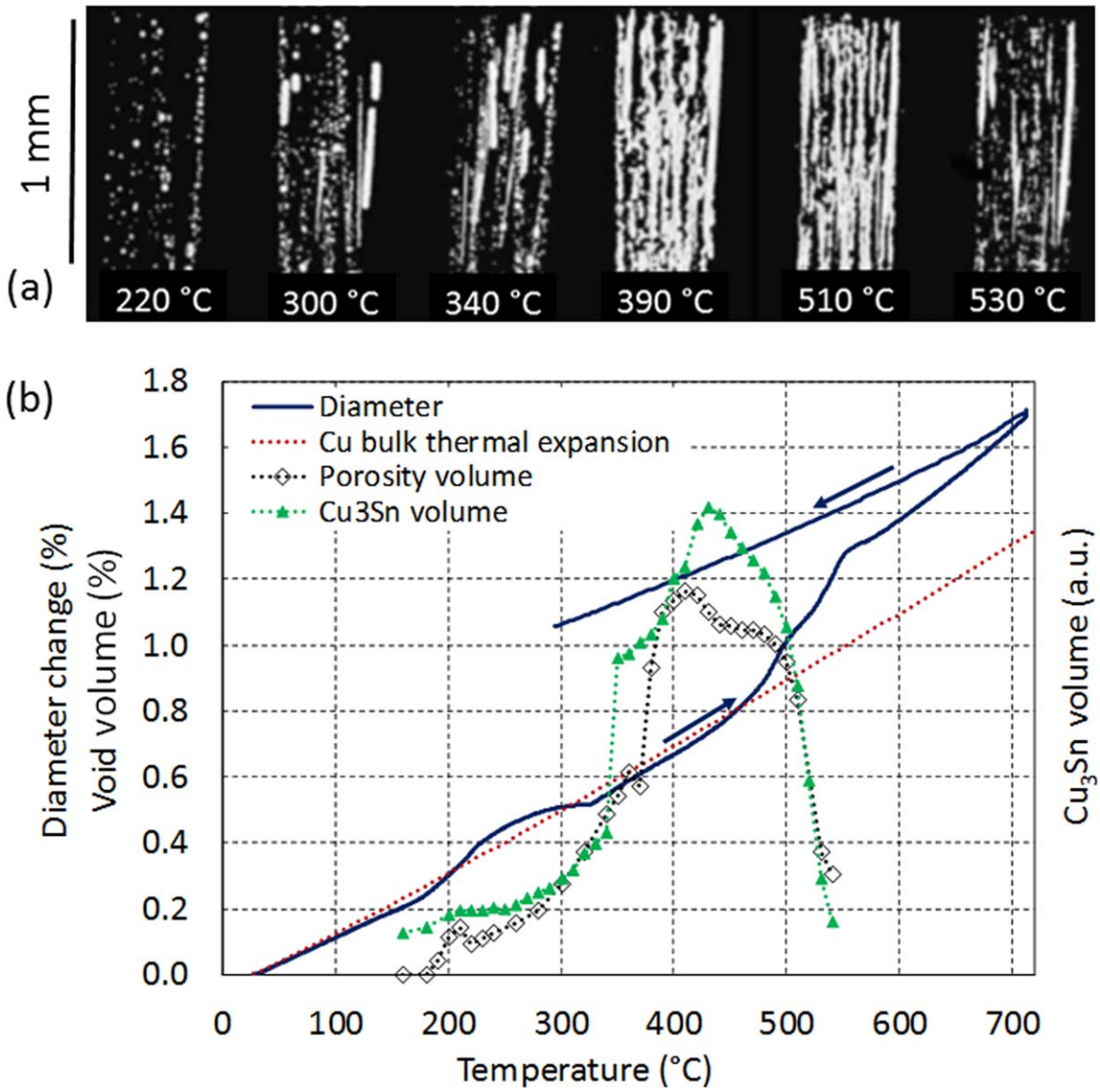

Figure 7. (a) 3D view of the pores in the IT wire recorded by μ-CT during *in situ* RHT (the strand materials have been transparently depicted). Reprinted from [19], with the permission of AIP Publishing. (b) Comparison of the IT wire diameter, pore volume and Cu_3Sn volume changes during RHT.

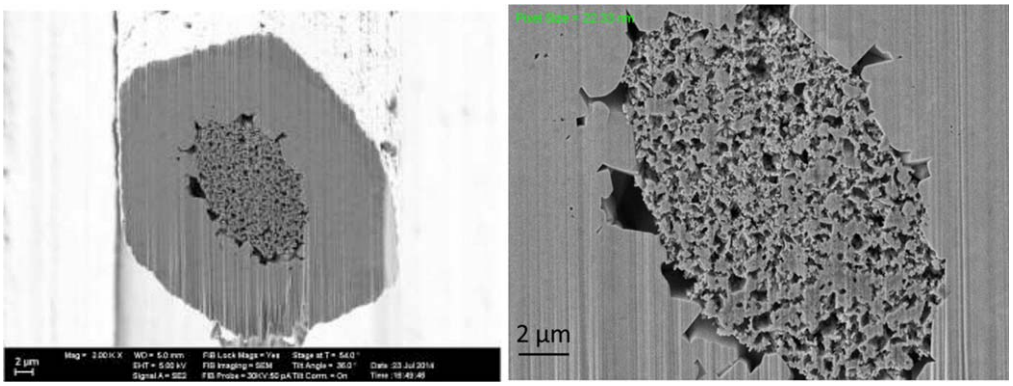

Figure 8. SEM transverse FIB cross-section of: (a) entire Nb_3Sn filament extracted from a fully processed PIT wire, and; (b) detailed view of the porosity in the filament core. A video showing the sequence of FIB nano-tomography slices through the PIT filament acquired with a distance of 65 nm is available[6].

filament cannot be visualized. In contrast, in cross-sections carefully prepared by the FIB technique the porosity is revealed (figure 8). The small pores in the PIT core center and larger pores between the coarse Nb_3Sn grains [33] are clearly resolved in the FIB-SEM images of the wire after a 34 h plateau at 695 °C. By acquiring a sequence of FIB-SEM images with a 65 nm distance between each slice, the pore distribution can be viewed in three dimensions.

The comparison of figure 8 with the μ-CT images of figures 6(a) and 7(a) illustrates the main advantages and disadvantages of the two tomographic techniques. The spatial resolution achievable by FIB-SEM nano-tomography is far superior to that of μ-CT. However, the field of view of FIB-SEM nano-tomography is limited, and the sample volume in the μ-CT images of figures 6(a) and 7(a) is three orders of magnitude larger.

FIB polishing artefacts continue to affect the view of the pores, and hamper the quantification of the pore volume. *In situ* studies to monitor pore evolution during RHT are not possible. Therefore, for the PIT wire we did not attempt quantification of the pore volume, and we cannot provide a comparison of the pore volume evolution with the PIT wire diameter evolution (figure 1). Nevertheless, it is clear from figure 8 that a significant pore volume remains in the core of a fully reacted PIT wire.

5. Discussion

5.1. Phase evolution during RHT of the IT, PIT, and RRP wires

The layout and overall composition of the three Nb_3Sn wires studied here differ strongly. The IT wire has comparatively low Sn content, and the diffusion distances are larger than in the other wires. Unlike the IT and RRP wires, in the PIT wire the precursor is present as a mixture of Sn and $NbSn_2$ particles, and only a relatively small amount of Cu is available inside the PIT subelement. These differences lead to markedly different phase evolutions during RHT, in particular at temperatures >450 °C, which could be monitored in great detail by combining state-of-the-art *in situ* XRD, μ-CT, and DSC experiments.

At temperatures below 450 °C the phase evolution in the three wire types is similar, with solid state interdiffusion of Cu and Sn, Cu_6Sn_5 formation, and Cu_6Sn_5 peritectic transformation, respectively. In all three wires an endothermic DSC signal is detected at around 227 °C, which corresponds to the eutectic transformation of the binary Cu-Sn phase diagram [29].

However, comparison of the DSC signals (figure 9) reveals some marked differences. The PIT wire shows the smallest peak area at 227 °C, due to the relatively low content of pure Sn precursor in the initial mixture, and the early solid state diffusion of Sn in Cu and Cu_6Sn_5 formation already in evidence at 130 °C by *in situ* XRD (figure 3).

[6] https://edms.cern.ch/document/1411539/1

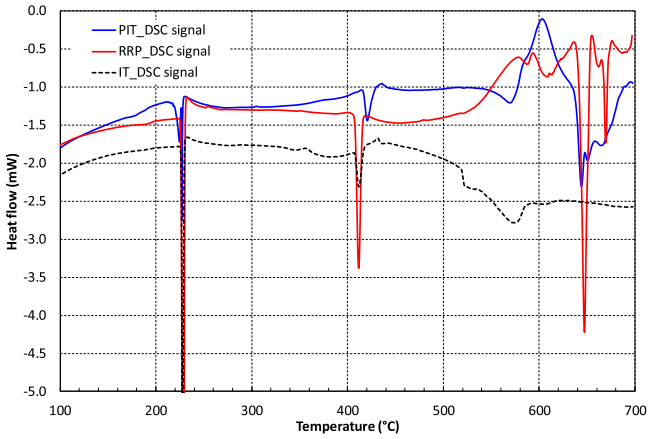

Figure 9. Comparison of the heat flow (ramp rate 5 °C min^{-1}) measured *in situ* by DSC for the IT, RRP, and PIT wires.

At around 410 °C the peritectic transformation of Cu_6Sn_5 occurs, according to reaction (1). The measured DSC peak temperatures for this transformation in the RRP and IT wires (411.5 °C and 411.8 °C, respectively) are in good agreement with the temperature of 408 °C predicted by the Cu-Sn binary phase diagram [29]. This states that low temperature (T < 450 °C) reactivity in RRP and IT wires is mainly driven by binary Sn-Cu reactivity. This is not the case for the PIT wire, where the Cu_6Sn_5 transformation was measured at 420 °C, suggesting that the presence of Nb shifts the transformation to a higher temperature.

The main differences in phase evolutions in the three wires are found at T > 450 °C. The main solid phase after Cu_6Sn_5 transformation is Cu_3Sn for IT and RRP wires (figures 2(b) and 5, respectively), whereas it is the ternary $(Nb_{0.75}Cu_{0.25})Sn_2$ compound that is detected for the PIT wire. Very marked differences are found for the Cu_3Sn XRD signal disappearance: between 430 °C and 530 °C for IT wire (figure 2(b)), between 530 °C and 600 °C for PIT wire (figure 3), and between 590 °C and 670 °C for RRP wire (figure 5). This cannot be explained by Cu_3Sn transformation at thermodynamic equilibrium, which in the binary Cu-Sn phase diagram occurs at 676 °C by congruent melting to form the Gamma phase [29]. This suggests that phase evolution in the different wires is driven by the liquid composition evolution in temperature with enrichment of mainly Cu. There is no direct measurement of Liquid composition in temperature, but the RRP and PIT wire phase formation sequence ($(Nb_{0.75}Cu_{0.25})Sn_2$ -> $NbSn_2$ -> Nb_6Sn_5 (figure 5)) is in very good agreement with the different phase equilibria formed in the Cu-Nb-Sn ternary phase diagram according to the liquid composition [32].

The phase evolution at higher temperatures is difficult to correlate to the DSC signal because of convoluted contributions. A huge exothermic peak is found at around 600 °C for the PIT wire (figure 3), and according to the phase detected by XRD it might only be attributed to $NbSn_2$ formation. It is probable that this exothermic contribution is also found in the RRP wire, where a comparatively smaller amount of $NbSn_2$ is formed, and might be hidden by endothermic contributions.

Strong and narrow endothermic peaks are detected at 647 °C and 644 °C for the RRP and PIT wires, respectively (figures 3 and 5), and might be correlated in both wires to the $NbSn_2$ -> Nb_6Sn_5 transformation involving liquid composition evolution. In the RRP wire a further sharp endothermic peak is detected at 669 °C, coinciding with the vanishing of Nb_6Sn_5 and Cu_3Sn as observed by the XRD measurements.

5.2. Volume and microstructure evolution during RHT of the IT, PIT, and RRP wires

The volume changes of Nb_3Sn wires during processing differ strongly from those expected from the thermal expansion coefficients of the their constituent materials. The initial length shrinkage of the RRP wire (figure 6) is typical for multifilament superconductor wires, and is caused by relaxation of the filament stress when the cold drawn Cu stabiliser is annealed during RHT [9]. The comparatively small wire length reduction can explain the first small diameter increase, but it cannot be the reason for the much stronger increase in wire cross-section at higher temperatures.

If the Nb_3Sn wire volume increase during RHT exceeds that caused by thermal expansion, it is always associated with porosity formation in the wire, since the density of Nb_3Sn and other intermetallics formed during RHT is higher than the weighted average of their precursor densities [10, 34, 35]. If void formation inside Nb_3Sn superconductors is suppressed by application of external pressure, for instance by hot isostatic pressure treatment, the diameter of the unreacted RRP wire can even be reduced during RHT [10].

However, the formation of void volume due to intermetallic formation does not necessarily cause an increase in wire diameter, as illustrated by the comparison of void space and diameter evolution of the IT wire. In the approximate temperature interval of 250–550 °C, the IT wire diameter increase does not exceed that caused by thermal expansion of its main constituent, Cu. The formation of porosity, which volume is 1.2% of the entire IT wire volume (figure 7), is due to the formation of Cu_3Sn, which has a comparatively high density [35]. The diameter of the IT wire starts to increase more than the Cu thermal expansion at the same temperature where the disappearance of Cu_3Sn is detected (above 450 °C). This suggests that the transformation of the high-density phase Cu_3Sn in lower density phases causes the increase in wire diameter.

The diameter increase of the unconfined RRP and PIT wires may be influenced by the formation of liquid. In the RRP wire the strongest diameter increase is observed when the temperature exceeds about 650 °C, which may be attributed to transformation of the high-density Cu_3Sn and the formation of Nb_3Sn. In the PIT wire the heating duration was insufficient to form a large amount of Nb_3Sn (figure 4).

The standard RHT cycle for 11 Tesla dipole coils is about eight days. Such long heat treatments cannot be realized for the *in situ* experiments described here, because of prohibitive cost and/or drift phenomena. Instead, accelerated heat treatments were applied, with ramp rates of about 100 °C h^{-1} without long plateaus. The modified and accelerated RHT cycles may shift the phase and microstructure changes to somewhat higher temperatures [36] and influence the absolute conductor expansion. However, at least for the RRP wire, where Nb_3Sn formation is the fastest, we believe that the qualitative behavior of conductor expansion as a function of temperature is representative for the full RHT cycle too. In order to obtain absolute values of conductor volume changes, the *in situ* results are complemented by *ex situ* measurements before and after the entire heat cycle (table 1).

During the RHT of an accelerator magnet coil the Rutherford cable conductor is confined, and the volume changes are influenced by the properties of the mould and of the other coil constituents. Future experiments will seek to measure the Nb_3Sn dipole coil segment expansion, using a stress–strain rig under transverse strain control, simulating the thermal expansion of the reaction mould and reproducing the stress conditions during coil RHT. In order to predict coil length changes, the resulting stresses and the friction coefficients of the relevant material pairs must be taken into account as well.

6. Conclusion

We have studied the endothermic and exothermic phase transformations and the volume changes during RHT of Nb_3Sn wires produced by three fabrication routes. With the advanced *in situ* materials characterisation methods that were applied, a detailed description of the phase and microstructure changes during Nb_3Sn wire processing has been obtained. Strong differences in phase evolutions in the different wires are found, in particular when temperatures exceed 450 °C. In combination with *in situ* dilation measurements, the complex Nb_3Sn wire volume change behavior could be associated with distinct phase changes.

The comparatively small length change that is typically observed after RHT of unconfined multifilament superconducting wires contributes slightly to increase in cross-section of the Nb_3Sn wire. The diameter evolution during RHT is characteristic for each Nb_3Sn wire type. The strongest volume increase, of about 5%, is observed in the RRP wire, where the main diameter change occurs above 600 °C and is related to Nb_3Sn formation. The strongest wire diameter increase measured in the IT wire is presumably caused by the transformation of the high-density phase Cu_3Sn in lower density phases.

Acknowledgments

We acknowledge the European Synchrotron (ESRF) for beam time at beamline ID15A. Thermal analysis experiments were performed at 'Plateforme Lyonnaise d'analyse thermique' (http://lmi.cnrs.fr/en/teams/plateforme_plat/).

ORCID iDs

C Scheuerlein https://orcid.org/0000-0002-8512-7187
J Andrieux https://orcid.org/0000-0003-2577-7214
M Michels https://orcid.org/0000-0003-0267-6154
F Lackner https://orcid.org/0000-0003-1670-4726

References

[1] Evans L (ed) 2009 *The Large Hadron Collider: A Marvel of Technology* (Lausanne: EPFL Press) 251
[2] Bottura L, de Rijk G, Rossi L and Todesco E 2012 Advanced accelerator magnets for upgrading the LHC *IEEE Trans. Appl. Supercond.* **22** 4002008
[3] Ambrosio G 2012 Nb_3Sn high field magnets for the high luminosity LHC upgrade project *IEEE Trans. Appl. Supercond.* **22** 4002107
[4] Abada A *et al* FCC-hh: the Hadron Collider *The European Physical Journal Special Topics* **228** 755–1107
[5] Schoerling D *et al* The 16 T dipole development program for FCC and HE-LHC *IEEE Trans. Appl. Supercond.* **29** 1–9
[6] Godeke A 2005 Performance boundaries in Nb_3Sn superconductors *PhD Thesis* University of Twente, Enschede, The Netherlands
[7] Ballarino A *et al* 2019 The CERN FCC conductor development program: a worldwide effort for the future generation of high-field magnets *IEEE Trans. Appl. Supercond.* **29** 6000709
[8] Martin S, Walnsch A, Nolze G, Leineweber A, Léaux F and Scheuerlein C 2017 The crystal structure of $(Nb_{0.75}Cu_{0.25})Sn_2$ in the Cu-Nb-Sn system *Intermetallics* **80** 16–21
[9] Dietderich D R, Litty J R and Scanlan R M 1998 Dimensional Changes of Nb_3Sn, Nb_3Al and $Bi_2Sr_2CaCu_2O_8$ conductors during heat treatment and their implication for coil design *Adv. Cryog. Eng.* B **44** 1013–20
[10] Scheuerlein C, Di Michiel M, Arnau G and Buta F 2008 Phase transformations during the reaction heat treatment of Internal Tin Nb_3Sn strands with high Sn content *IEEE Trans. Appl. Supercond.* **18** 1754–60
[11] Michels M, Lackner F, Scheuerlein C, Carlon Zurita A, Ferradas Troitino S, Bourcey N, Savary F and Tommasini D 2019 Length changes of unconfined Nb_3Sn Rutherford cables during reaction heat treatment *IEEE Trans. Appl. Supercond.* **29** 6000605
[12] Savary F *et al* 2015 Status of the 11 T Nb_3Sn dipole project for the LHC *IEEE Trans. App. Supercond.* **25** 4003205
[13] Vallone G 2018 Mechanical design analysis of MQXFB, the 7.2 m long low-β quadrupole for the high luminosity LHC upgrade *IEEE Trans. Appl. Supercond.* **28** 4003705
[14] Scheuerlein C, Lackner F, Savary F, Rehmer B, Finn M and Uhlemann P 2017 Mechanical properties of the HL-LHC 11 Tesla Nb_3Sn magnet constituent materials *IEEE Trans. Appl. Supercond.* **27** 4003007
[15] Scheuerlein C, Lackner F, Savary F, Rehmer B, Finn M and Meyer C 2018 Thermomechanical behavior of the HL-LHC 11 Tesla Nb_3Sn magnet coil constituents during reaction heat treatment *IEEE Trans. Appl. Supercond.* **28** 4003806
[16] Scheuerlein C, Gan W M, Hofmann M and Katzer B 2019 Texture in superconducting magnet constituent materials and its effect on elastic anisotropy *IEEE Trans. Appl. Supercond.* **29** 7800105
[17] Scheuerlein C, Wolf F, Lorentzon M and Hofmann M 2019 Direct measurement of Nb_3Sn filament loading strain and stress in accelerator magnet coil segments *Supercond. Sci. Technol.* **32** 045011 (7pp)
[18] Durante M, Bredy P, Devred A, Otmani R, Reytier M, Schild T and Trillaud F 2001 Development of a Nb_3Sn multifilamentary wire for accelerator magnet applications *Physica* C **354** 449–53
[19] Scheuerlein C, Di Michiel M and Haibel A 2007 On the formation of voids in Nb_3Sn superconductors *Appl. Phys. Lett.* **90** 132510
[20] Parrell J A, Zhang Y, Field M B, Cisek P and Hong S 2003 High field Nb_3Sn conductor development at Oxford superconducting technology *IEEE Trans. Appl. Supercond.* **13** 3470–3
[21] Thilly L, Di Michiel M, Scheuerlein C and Bordini B 2011 Nb_3Sn nucleation and growth in multifilament superconducting strands monitored by high resolution synchrotron diffraction during *in situ* reaction *Appl. Phys. Lett.* **99** 122508
[22] Lindenhovius J L H, Hornsveld E M, den Ouden A, Wessel W A J and ten Kate H H J 2000 *IEEE Trans. Appl. Supercond.* **10** 975–8
[23] Di Michiel M and Scheuerlein C 2007 Phase transformations during the reaction heat treatment of powder-in-tube Nb_3Sn superconductors *Supercond. Sci. Technol.* **20** L55–8
[24] Scheuerlein C, Di Michiel M and Buta F 2009 Synchrotron radiation techniques for the characterisation of Nb_3Sn superconductors *IEEE Trans. Appl. Supercond.* **19** 2653–6
[25] Di Michiel M, Merino J M, Fernandez-Carreiras D, Buslaps T, Honkimäki V, Falus P, Martins T and Svensson O 2005 Fast microtomography using high energy synchrotron tomography *Rev. Sci. Instrum.* **76** 043702
[26] Jacques S D M, Di Michiel M, Beale A M, Sochi T, O'Brien M G, Espinosa-Alonso L, Weckhuysen B M and Barnes P 2011 Dynamic x-ray diffraction computed tomography reveals real time insight into catalyst active phase evolution *Angew. Chem. Int. Ed.* **50** 10148–52
[27] McRae D M and Walsh R P 2013 Dimensional changes of Nb_3Sn conductors and conduit alloys during reaction heat treatment *IEEE Trans. Appl. Supercond.* **23** 9000404
[28] Bocian D, Ambrosio G and Wilson G M 2012 Measurements of Nb_3Sn conductor dimension changes during heat treatment *AIP Conf. Proc.* **1435** 193–200
[29] Fürtauer S, Li D, Cupid D and Flandorfer H 2013 The Cu-Sn phase diagram, Part I: new experimental results *Intermetallics* **34** 142–7
[30] Lee B J 2002 Prediction of interfacial reactions using thermodynamic calculation and diffusion simulation *TMS Annual Meeting* 131–44
[31] Perrot P and Schuster J C Copper-niobium-tin *Landolt-Börnstein, New series IV (Physical Chemistry), Volume 11 (Ternary Alloys Systems), Sub-volume C (Non-ferrous Metal systems), Part 2 (Selected Copper Systems* ed G Effenberg and S Ilyenko (Berlin: Springer) 364–73
[32] Li M, Du Z, Guo C and Li C 2009 Thermodynamic optimization of the Cu–Sn and Cu–Nb–Sn systems *J. Alloys Compd.* **477** 104–17
[33] Segal C *et al* 2016 Evaluation of critical current density and residual resistance ratio limits in powder in tube Nb_3Sn conductors *Supercond. Sci. Technol.* **29** 085003
[34] Kapoor D and Wright R N 1980 Structural characteristics of Nb_3Sn produced by three P/M techniques *Metallurgical Trans.* A **11A** 685–92
[35] Fields R J, Low S R and Lucey G K Jr Physical and mechanical properties of intermetallic compounds commonly found in solder joints http://metallurgy.nist.gov/mechanical_properties/solder_paper.html
[36] Sanabria C *et al* 2018 Controlling Cu–Sn mixing so as to enable higher critical current densities in RRP® Nb_3Sn wires *Supercond. Sci. Technol.* **31** 064001 2018 Supercond. Sci. Technol. 31 064001